Energy absorption of discretely assembled composite self-locked systems

Jinxin Pan [a,b,1], Weiyu Zhu [a,1], Kuijian Yang [a,*], Lingling Hu [a], Yuli Chen [c]

[a] Department of Applied Mechanics & Engineering, Sun Yat-sen University, Guangzhou 510275, PR China
[b] State Key Laboratory of Nonlinear Mechanics, Chinese Academy of Sciences, Beijing 100190, PR China
[c] Institute of Solids Mechanics, Beihang University, Beijing 100191, PR China

ARTICLE INFO

ABSTRACT

Impact accidents cause great damage to lives and devices due to strong destructiveness and weak predictability, and accordingly, flexibility and modifiability are essential in the design of novel impact-resistant structures. To achieve this goal, two newly-designed energy absorption systems were proposed in this paper, which could be discretely assembled without boundary constraints. Quasi-static experiments and finite element method (FEM) simulations were carried out to reveal the deformation mechanism and test the usability, based on which the analytical solutions of the crushing force of the models were established adopting plastic hinge analysis and energy method. Parametric study of multiple-tube systems was conducted to reveal the effects of foam porosity and inner tube parameters on dynamic response, and the optimal design was summarized, achieving the energy absorption efficiency of 39%. The functionally graded design of composite self-locked (CSL) systems was explored, and it was proven that the system with positive stiffness gradient was optimal.

1. Introduction

Sudden impacts cause severe damage to lives and properties, and accordingly, the development of effective energy absorption devices plays a paramount role in many fields, including aerospace, road traffic and navigation [1–3]. Thin-walled structures possess superior impact-resistant energy absorption performance because of light weight and high specific modulus [4–6], and among them round tube system is most widely used in engineering applications [7–9]. However, complicated boundary constraints are required before application to avoid the lateral splash of round tubes under impacts. The square- and ellipse-shaped tubes had been proven to respectively promote energy absorption capacity and efficiency by increasing material utilization [10,11], and nested systems were proposed by inserting inner tubes or rods to improve space utilization, while the energy-absorbing efficiency was commonly impaired owing to the distinct increase of overall stiffness [12,13]. Honeycomb structures, lattice structures, foaming materials and composite structures had also been studied extensively due to stable performance and enhanced designability [14–17].

Considering the urgency of impact accidents, the modifiability is in great demand for energy absorption systems to reduce the preparing time. Nevertheless, complicated boundary constraints are required for traditional energy-absorbing structures to ensure overall stability, which severely impairs the flexibility to response quickly to emergencies. Furthermore, once manufactured as a continuum, the characteristics parameters and arrangement patterns of the elements cannot be adjusted flexibly to meet the particular protection requirements, and the overall structure tends to be scrapped when some elements have already been crushed. To solve this problem, discretely assembling based on modular concept without the need of external constraints is the key [18]. Recently, Chen et al. proposed a self-locked energy absorption system [19], in which tubes can interlock with each other after discretely assembling, and the initial force peak was attenuated effectively due to special topology design [20] (Supplementary Material S1). However, the material and space utilizations require further improvement, and the effect of graded design relying on tube thickness control is limited, making it difficult to achieve expected properties of continuum body.

To enhance impact-resistant performance as well as improving modifiability and designability, two discretely assembled energy absorption systems, including composite self-locked (CSL) and nested composite self-locked (NCSL) models, were proposed in this paper. Quasi-static experiments and FEM simulations were firstly carried out to test the energy absorption response of the newly-designed models, and

---

then the analytical solutions of the crushing force of models were derived based on plastic hinge analysis and energy method, to reveal the effect of deformation mechanism on energy-absorbing performance. Then, parametric study of multiple-tube systems under dynamic loading condition was conducted, where the effects of foam porosity and inner tube parameters were successively discussed and the optimal design was summarized. Finally, the dynamic response of CSL multiple-tube systems with various stiffness graded designs was investigated, and it was proven that the system with positive stiffness gradient was optimal under various loading conditions. This work provides guidelines for the design of energy-absorbing structures, and opens a new avenue for theoretically analyzing the mechanical response of composite structures.

2. Experimental study

Tube specimens of different models with various foam porosities are fabricated and assembled, and experiments and FEM simulations are carried out to compare their energy absorption response.

2.1. Tube specimens and experimental setups

Traditional thin-walled hollow self-lock (HSL) tube specimens are manufactured by three-dimensional printing method using 316L stainless steel as shown in Fig. 1(a), which is comprised of two cylindrical shells on both sides and two middle connecting plates. The tube geometry is determined by 5 parameters: the axial length L, the flat plate width W, the spacing between the flat plates S, the thickness T and the mean diameter of cylindrical shells D. The average mass of HSL specimens is 165.5 g, with material and geometry parameters respectively listed in Tables 1 and 2.

To enhance impact-resistant performance as well as improving modifiability and designability, two innovative tube models are proposed in this study by inserting cylindrical aluminum foam and round inner tubes into the two cylindrical shells of HSL model, including composite self-lock (CSL) model and nested composite self-lock (NCSL) model as shown in Fig. 1(b)–(c). The aluminum foam filler is adopted as closed-cell foam and prepared by smelt foaming method, where the foam porosity is denoted by θ. Herein, the porosities of aluminum foam specimens are adopted as 89.6% and 84.6%, respectively corresponding to equivalent density of 280.8 kg/m³ and 415.8 kg/m³. The nominal stress–strain diagrams of foam specimens are obtained from compressive tests, as shown in Fig. S4 (Supplementary Material S2). The inner tube specimens are manufactured using 304 stainless steel, with mechanical properties provided in Table 1. The axial length of foam filler and inner tubes are both selected as L, and the mean diameter and thickness of

inner tubes are respectively denoted by d and t for NCSL model. The average parameters of single cylindrical aluminum foam and round inner tube of CSL and NCSL specimens are provided in Table 3.

The quasi-static crushing of the experimental specimens of HSL, CSL1, CSL2, NCSL1 and NCSL2 models is conducted by MTSE 45.305 test machine, and each specimen is placed between loading and supporting plates, as shown in Fig. 3. The supporting plate is fixed, and the loading plate crushes the specimen with constant speed of 1 mm/min, which is low enough to reduce dynamic effects. The measuring range of the load cell is up to 300kN, with accuracy of 0.5%. The load and the corresponding displacement of the loading plate are recorded per 0.05 s, and the deformed configurations of the specimens are recorded by high definition camera.

2.2. Mechanical response

The crushing force of the five models obtained from experiments are depicted as solid symbols in Fig. 2(a), where the crushing displacement u is normalized by the initial height of the models in compressive direction

Table 1
Material properties of stainless steel.

Type	Young's modulus E (GPa)	Poisson ratio ν	Yield stress σ_s (MPa)	Hardening modulus E_p (MPa)	Density ρ_s (kg/m³)
316L	206	0.3	360	1100	7980
304	189	0.25	340	1100	7930

Table 2
Average geometric parameters of HSL specimens (mm).

Axial length L	Plate width W	Plate spacing S	Wall thickness T	Mean diameter D
100.0	34.8	2.9	1.1	21.1

Table 3
Average parameters of fillers of CSL and NCSL specimens.

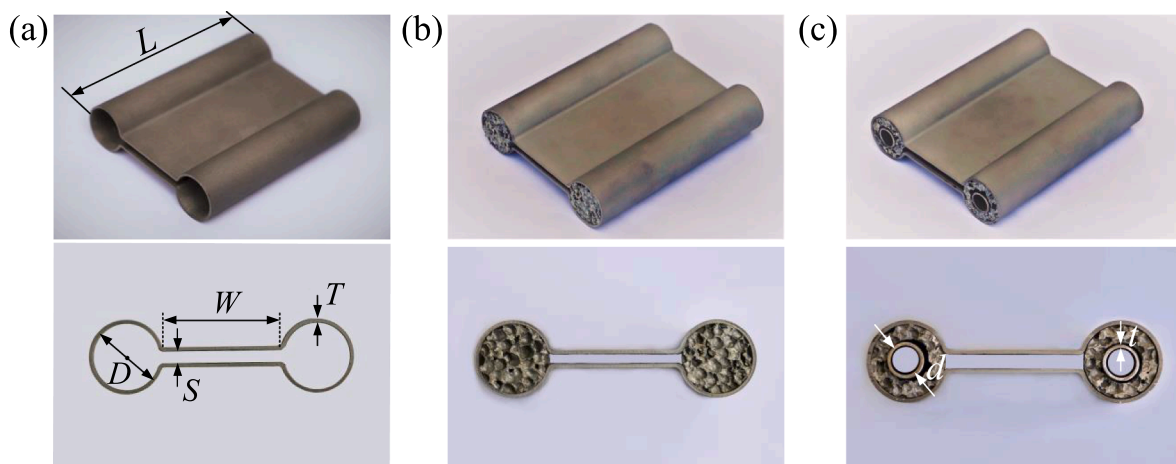| Model	Cylindrical Aluminum foam			Round inner tube		
	Porosity θ (%)	Mass m_{foam} (g)		Diameter d (mm)	Thickness t (mm)	Mass m_{inner} (g)
CSL1	89.6	17.6		/	/	/
CSL2	84.6	26.1		/	/	/
NCSL1	89.6	13.2		8.9	1.1	48.8
NCSL2	84.6	19.6		8.9	1.1	48.8

Fig. 1. Isometric view and side view of specimens: (a) hollow self-lock (HSL), (b) composite self-lock (CSL) and (c) nested composite self-lock (NCSL) models.
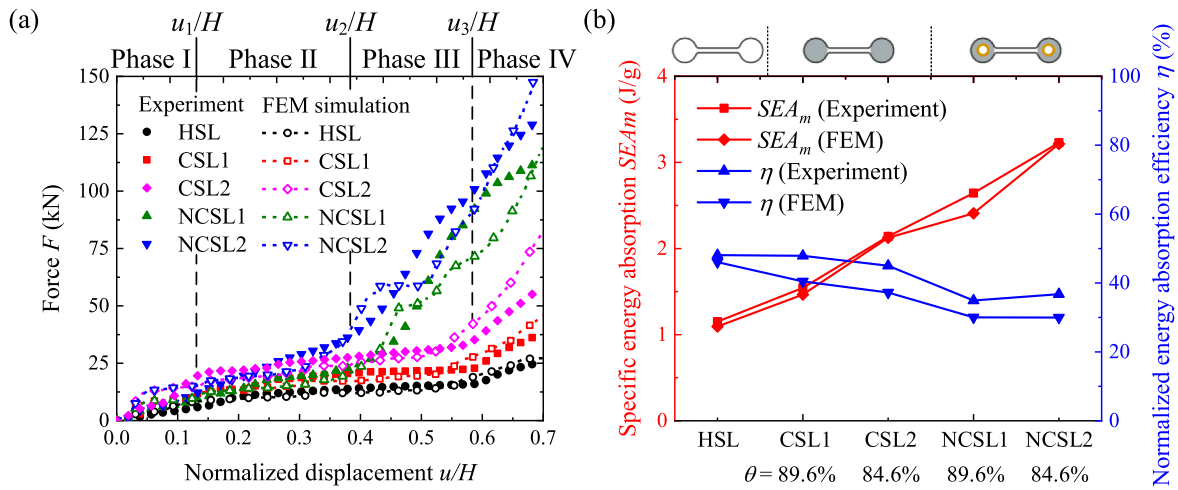
Fig. 2. Mechanical response of HSL, CSL and NCSL models with various foam porosity: (a) force–displacement curves and (b) key performance indicators.
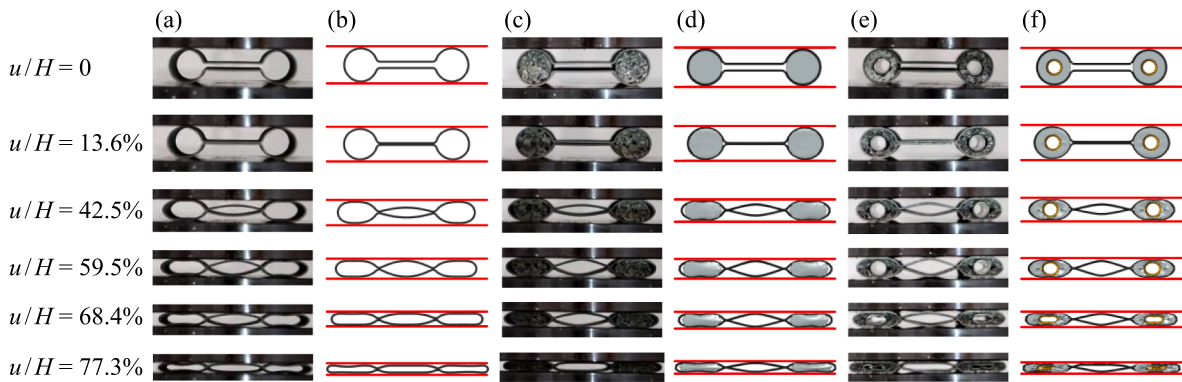

Fig. 3. Deformed configurations of (a)–(b) HSL model, (c)–(d) CSL1 model and (e)–(f) NCSL1 model obtained from experiments and FEM simulations.

$H = D + T$. To reveal the effect of deformation mechanism on mechanical response, the experimental deformed configurations of HSL, CSL1 and NCSL1 models are displayed in Fig. 3(a), (c) and (e) as instances. The FEM simulation is also carried out by ABAQUS/Explicit, with details in Supplementary Material S2. In the simulation, the tube parameters and loading conditions are exactly same as those in experiment to make a comparison. The numerical force–displacement curves of the five models are presented as dashed lines with hollow symbols in Fig. 2(a), and the deformation process is recorded in Fig. 3(b), (d) and (f).

As shown in Fig. 3(a) and (b), the deformation of HSL model presents a three-phase behavior. In phase I, upper and lower sides of cylindrical shells are flattened and respectively attached to the loading and supporting plates, and the middle plates are getting close to each other. As the crushing progresses, the middle plates of the tube contact each other at about 13.6% normalized displacement, and the deformation of the tube enters phase II. The flattened zones of cylindrical shells are enlarged significantly, and the middle plates begin bending reversely. At about 59.5% normalized displacement, the upper and lower middle plates respectively touch the loading and supporting plates, and the deformation enters the final phase. In the final phase, the middle plates are gradually flattened and attached to the loading and supporting plates, and the tube deformation is increasingly severe until the model

completely loses the energy absorption potentials. For CSL model, due to strong load-carrying capacity and high squeezability of aluminum foam, the force–displacement curve is obviously higher than HSL model, and the deformation process is basically the same. For NCSL model, the foam filler is highly densified at about 35%-45% normalized displacement, when the inner tubes start resisting the compressive load. Therefore, the force–displacement curve of NCSL model presents a sudden increase here, and thus displays a four-phase deformation process.

Overall, the experimental and simulation results of HSL model coincide well with each other, and the deformation is nearly longitudinal symmetrical. The difference between experimental and simulation results is mainly caused by the manufacturing error of specimens and ideal assumptions of material constitutive relations. The upper and lower halves of HSL specimen occur slight horizontal sliding, and thus the final deformed process of specimen occurs later than simulation and the maximum experimental force is significantly smaller than that obtained from FEM simulation. Besides, the steel is adopted as bilinear elastic–plastic constitutive model and the aluminum foam is adopted as crushable foam model, which slightly differs from behavior of real material of specimen.

Herein, the deformation phases of NCSL models are defined as phases I-IV, and the displacement between i-th and $i + 1$-th phases of NCSL model is denoted by u_i ($1 \leq i \leq 3$), as shown in Fig. 2(a).The critical

displacements u_1 and u_2 are approximated as (Supplementary Material S3).

$$\begin{cases} u_1 = S \\ u_2 = (D - T - d - t)\theta \end{cases} \tag{1}$$

and the approximate solution of u_3 can be obtained from (Supplementary Material S3).

$$(H - u_3)\left(\arcsin\frac{u_3}{H} - \arcsin\frac{S}{H}\right) = W\left[1 - \cos\left(\arcsin\frac{u_3}{H} - \arcsin\frac{S}{H}\right)\right] \tag{2}$$

The accuracy of Eqs. (1) and (2) are validated by FEM simulation (Supplementary Material S3).

2.3. Key performance indicators

In this paper, the specific energy absorption SEA_m and normalized energy absorption efficiency η are adopted as key performance indicators. The effective stroke ratio is taken as $ESR = S_{ef}/H = 0.7$ [21], where S_{ef} is the effective stroke. The total energy absorption EA can be calculated by.

$$EA = \int_0^{0.7H} F \mathrm{d}u \tag{3}$$

The specific energy absorption SEA_m is defined as the energy absorption per unit mass.

$$SEA_m = \frac{EA}{m} \tag{4}$$

where m is the mass of the model. For single tube model, it is satisfied that.

simulations are calculated and displayed in Fig. 2(b). The specific energy absorption SEA_m obtained from experiments and FEM simulations coincide well with each other, and the experimental normalized energy absorption efficiency η is slightly larger than that of FEM simulation because of manufacturing error. From the results in Fig. 2, the composite design can obviously enhance the load-carrying capacity, among which NCSL models display largest SEA_m, and the energy absorption capacity can be increasingly enlarged by decreasing the foam porosity. For instance, NCSL2 model displays SEA_m two times larger than that of HSL model. Because the maximum force is also increased, η of the proposed models is weakened compared with HSL model. Even so, the loss of energy absorption efficiency can be impaired by decreasing inner tube thickness or selecting suitable foam porosity, which will be proven in Section 4.

3. Theoretical model

To predict the energy absorption performance of the proposed models, a theoretical static model is proposed in this section. It is proven that the interaction effect of composite structure [23] can be ignored when subjected to lateral loads (Supplementary Material S4), and thus the crushing force of complete model can be approximated as the summation of forces of all single elements [24].
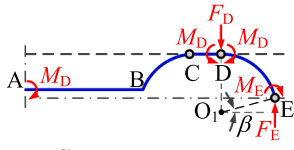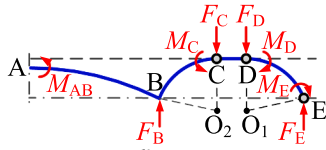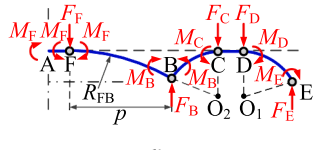
For thin-walled outer tube and inner tubes made by base metal, the mechanical response can be analyzed by plastic hinge model, where plastic deformation is assumed only occurring at the plastic hinges. Since elastic strain in metals is of the order of 0.001, whereas the effective stroke ratio is 70%, it is reasonable to neglect the elastic deformation process. The rigid-plastic model with isotropic linear hardening is adopted here to describe the constitutive relation of material [11,25].

$$\begin{cases} m_{\mathrm{HSL}} = 2\rho_{out}LT\left[W + D\left(\pi - \arcsin\frac{S}{D}\right)\right] \\ m_{\mathrm{CSL}} = 2\rho_{out}LT\left[W + D\left(\pi - \arcsin\frac{S}{D}\right)\right] + \frac{\pi\rho_{foam}L(D-T)^2}{2} \\ m_{\mathrm{NCSL}} = 2\rho_{out}LT\left[W + D\left(\pi - \arcsin\frac{S}{D}\right)\right] + \frac{\pi\rho_{foam}L\left[(D-T)^2 - (d+t)^2\right]}{2} + 2\pi\rho_{in}Ltd \end{cases} \tag{5}$$

where ρ_{out}, ρ_{foam} and ρ_{in} are respectively defined as the densities of outer tube material, aluminum foam filler and inner tube material. Herein, the density of aluminum foam filler can be calculated by.

$$\rho_{foam} = \rho_{\mathrm{Al}}(1 - \theta) \tag{6}$$

where ρ_{Al} is the density of homogeneous aluminum equaling 2.7 g/cm^3. The normalized energy absorption efficiency η is defined as the ratio of the mean load F_{mean} [22] to the maximum load F_{max}.

$$\eta = \frac{F_{mean}}{F_{max}} = \frac{EA}{0.7HF_{max}} \tag{7}$$

where F_{max} is adopted between $u = 0$ and $u = 0.7H$. The energy absorption properties of the five models in experiments and FEM

$$M = M_0\left(1 + \frac{E_p t_0}{3\sigma_s}\cdot k\right) \tag{8}$$

where $M_0 = \sigma_s t_0^2 L_0/(2\sqrt{3})$ is the yield moment, t_0 and L_0 are wall thickness and axial length, and k is the curvature calculated by $k = \alpha/(4t_0)$ [11], where α is the inclined angle.

The location of plastic hinges is firstly assumed, where only a quarter of the model is considered here because of symmetry. Geometry, moment and equilibrium equations are then established in Table 4, to obtain the analytical solution of the crushing force of outer tube F_{out}, which can be derived as.

Table 4
Theoretical model and core equations of the outer tube in each phase.

Analysis	Phase I ($0 \leqslant u_{out} < u_1$)	Phase II ($u_1 \leqslant u_{out} < u_3$)	Phase III ($u_3 \leqslant u_{out} < D-T$)
Theoretical model			
eometry equation	$\sin\beta = \dfrac{u_{out}}{D}$	$\sin\beta = \dfrac{u_{out}}{D}$ $$k_{AB} = \frac{2}{W}\left(\arcsin\frac{u_{out}}{D} - \arcsin\frac{S}{D}\right)$$	$\sin\beta = \dfrac{u_{out}}{D}$ $$k_{FB} = \frac{2}{W}\left(\arcsin\frac{u_3}{D} - \arcsin\frac{S}{D}\right)$$ $$\Delta k_F = \frac{2}{W}\left(\arcsin\frac{u_3}{D} - \arcsin\frac{S}{D}\right)$$ $$\Delta k_B = \frac{1}{4T}\left(\arccos\frac{2R_{FB}-D+u_3}{2R_{FB}}\right.$$ $$-\arccos\frac{2R_{FB}-D+u_{out}}{2R_{FB}}$$ $$\left.+\arcsin\frac{u_{out}}{D} - \arcsin\frac{u_3}{D}\right)$$ $$R_{FB} = \frac{W}{2}\left(\arcsin\frac{u_3}{D} - \arcsin\frac{S}{D}\right)^{-1}$$ $$p = \sqrt{R_{FB}^2 - \left(R_{FB} - \frac{D}{2} + \frac{u_{out}}{2}\right)^2}$$
Moment equation	$M_D = M_0\left(1 + \dfrac{E_p T}{3\sigma_s}\cdot\dfrac{2}{D}\right)$ $M_E = M_0\left(1 + \dfrac{E_p T}{3\sigma_s}\dfrac{2\beta}{4T}\right)$	$M_{AB} = M_0\left[1 + \dfrac{E_p T}{3\sigma_s}\cdot k_{AB}\right]$ $M_C = M_0\left(1 + \dfrac{E_p T}{3\sigma_s}\dfrac{2}{D}\right)$	$M_F = M_0\left[1 + \dfrac{E_p T}{3\sigma_s}\cdot(k_{FB}+\Delta k_F)\right]$ $M_B = M_0\left(1 + \dfrac{E_p T}{3\sigma_s}\cdot(k_{FB}+\Delta k_B)\right)$
Equilibrium equation	$F_D\cdot\dfrac{D}{2}\cos\beta = M_D + M_E$ $F_{out} = 2F_D$	$F_C\cdot\dfrac{D}{2}\cos\beta = M_{AB} + M_C$ $F_D\cdot\dfrac{D}{2}\cos\beta = M_D + M_E$ $F_{out} = 2(F_C + F_D)$	$F_C\cdot\dfrac{D}{2}\cos\beta = M_B + M_C$ $F_F\cdot p = M_F + M_B$ $F_{out} = 2(F_C + F_D + F_F)$

$$
F_{out} = \begin{cases}
\dfrac{4\sigma_{s,out}LT^2}{\sqrt{3(D^2 - u_{out}^2)}}\left(1 + \dfrac{E_{p,out}T}{3\sigma_{s,out}D} + \dfrac{E_{p,out}}{12\sigma_{s,out}}\arcsin\dfrac{u_{out}}{D}\right) \\
\qquad\qquad (0 \leqslant u_{out} < u_1) \\[2mm]
\dfrac{2\sigma_{s,out}LT^2}{\sqrt{3(D^2 - u_{out}^2)}}\left\{4 + \dfrac{E_{p,out}T}{3\sigma_{s,out}D}\left[4 + \dfrac{2D}{W}\left(\arcsin\dfrac{u_{out}}{D} - \arcsin\dfrac{S}{D}\right) + \dfrac{D}{2T}\arcsin\dfrac{u_{out}}{D}\right]\right\} \\
\qquad\qquad (u_1 \leqslant u_{out} < u_3) \\[2mm]
\dfrac{2\sigma_{s,out}LT^2}{\sqrt{3(D^2 - u_{out}^2)}}\left\{4 + \dfrac{E_{p,out}T}{3\sigma_{s,out}D}\left[4 + \dfrac{2D}{W}\psi + \dfrac{D}{4T}\left(3\arcsin\dfrac{u_{out}}{D} - \arcsin\dfrac{u_3}{D}\right.\right.\right. \\
\qquad\left.\left.\left. +\arccos\dfrac{W - (D - u_3)\psi}{W} - \arccos\dfrac{W - (D - u_{out})\psi}{W}\right)\right]\right\} \\
\qquad +2\sigma_{s,out}LT^2\psi\left[3W^2 - 3(W - D\psi + u_{out}\psi)^2\right]^{-\frac{1}{2}} \\
\qquad \cdot\left\{2 + \dfrac{E_{p,out}T}{3\sigma_{s,out}D}\left[\dfrac{6D\psi}{W} + \dfrac{D}{4T}\left(\arcsin\dfrac{u_{out}}{D} - \arcsin\dfrac{u_3}{D}\right.\right.\right. \\
\qquad\left.\left.\left. +\arccos\dfrac{W - (D - u_3)\psi}{W} - \arccos\dfrac{W - (D - u_{out})\psi}{W}\right)\right]\right\} \\
\qquad\qquad (u_3 \leqslant u_{out} < D - T)
\end{cases}
\tag{9}
$$

where u_{out}, $\sigma_{s,out}$ and $E_{p,out}$ are respectively the crushing displacement, yield stress and hardening modulus of the outer tube, and $\psi = \arcsin(u_3/D) - \arcsin(S/D)$.

Similarly, the crushing force of single inner round tube F_{in} can be derived as.

$$F_{in} = \frac{4\sigma_{s,in}Lt^2}{\sqrt{3(d^2 - u_{in}^2)}}\left(1 + \frac{E_{p,in}t}{3\sigma_{s,in}d} + \frac{E_{p,in}}{12\sigma_{s,in}}\arcsin\frac{u_{in}}{d}\right) \quad (10)$$

where u_{in}, $\sigma_{s,in}$ and $E_{p,in}$ are respectively defined as the crushing displacement, yield stress and hardening modulus of the inner tube. The accuracy of Eqs. (9) and (10) are validated by the experimental and simulation results (Supplementary Material S5). From the results, the analytical solutions of F_{out} and F_{in} coincide well with experimental and simulation results before densification stage. At large crushing displacement, the theoretical prediction gradually goes lower than the experimental and simulation results, which is caused by the assumption of plastic hinge model [26].

The deformation of aluminum foam is assumed consisting of plateau stress phase and densification phase, where σ_{pl} is the plateau stress and

ε_d is the densification strain. The energy absorption per unit equivalent volume $SEA_{V,foam}$ can be derived based on energy method [27].

$$SEA_{V,foam} = \begin{cases} \dfrac{\sigma_{pl}u_{foam}}{D-T} & (u_{foam} \leqslant u_d) \\[2ex] \dfrac{\sigma_{pl}u_{foam}}{D-T} + \dfrac{m}{n+1}\left(\dfrac{u_{foam}}{D-T} - \varepsilon_d\right)^{n+1} & (u_{foam} > u_d) \end{cases} \quad (11)$$

(Supplementary Material S6), where m and n are constants determined by experiment results in Fig. S4, u_{foam} is the crushing displacement of foam, and $u_d = (D-T)\varepsilon_d$ is the densification displacement. The real-time equivalent volume of foam cylinder in CSL and NCSL models can be expressed as.

$$V_{eq,foam-CSL} = \frac{L(D-T-u_{foam})}{2}\sqrt{2(D-T)u_{foam} - u_{foam}^2}$$
$$+\frac{L(D-T)^2}{2}\text{arctg}\frac{\sqrt{2(D-T)u_{foam} - u_{foam}^2}}{D-T-u_{foam}} \quad (12)$$

and

$$V_{eq,foam-NCSL} = \begin{cases} L\left\{\frac{\pi}{4}(D-T)^2\left(1 - \frac{2}{\pi}\arcsin\frac{D-T-u_{foam}}{D-T}\right)\right. \\[2ex] +\frac{D-T-u_{foam}}{2}\sqrt{2(D-T)u_{foam} - u_{foam}^2} - \frac{\pi}{4}(d+t)^2 \\[2ex] +\frac{(d+t)^2}{2}\arccos\frac{\sqrt{2(D-T)u_{foam} - u_{foam}^2}}{d+t} \\[2ex] \left.-\frac{\sqrt{\left(2(D-T)u_{foam} - u_{foam}^2\right)\left[(d+t)^2 - 2(D-T)u_{foam} + u_{foam}^2\right]}}{2}\right\} \\[2ex] (u_{foam} \leqslant u_{cr}) \\[2ex] L\left[\frac{\pi}{4}(D-T)^2\left(1 - \frac{2}{\pi}\arcsin\frac{D-T-u_{foam}}{D-T}\right)\right. \\[2ex] \left.+\frac{D-T-u_{foam}}{2}\sqrt{2(D-T)u_{foam} - u_{foam}^2} - \frac{\pi}{4}(d+t)^2\right] \\[2ex] (u_{foam} > u_{cr}) \end{cases} \quad (13)$$
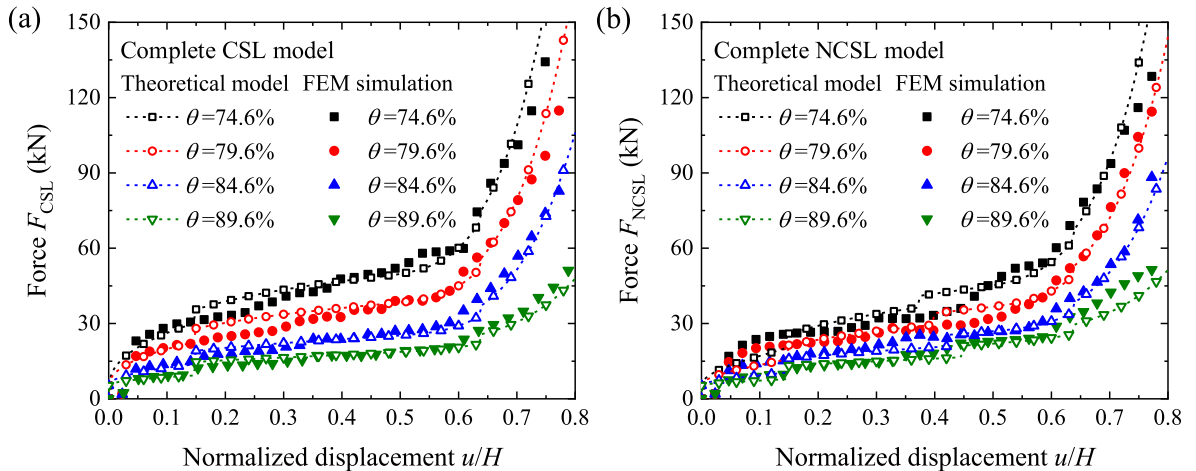

Fig. 4. The crushing force of (a) complete CSL model and (b) complete NCSL model with various foam porosities obtained from theoretical analysis and FEM simulation.
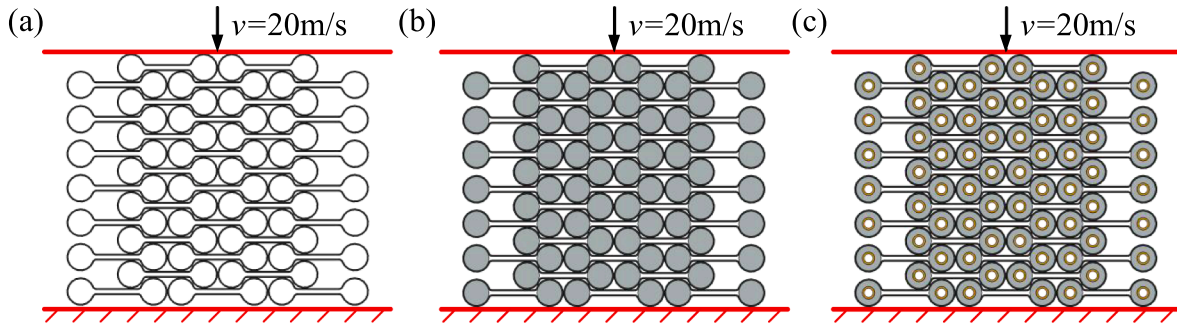
Fig. 5. Initial configurations of (a) hollow self-locked (HSL), (b)composite self-locked (CSL) and (c) nested composite self-locked (NCSL) systems under dynamic loading conditions ($v = 20$ m/s).

respectively (Supplementary Material S6). The critical displacement u_{cr} here is defined as the critical displacement in calculating $V_{eq,foam\text{-}NCSL}$, which can be expressed as.

$$u_{cr} = D - T - \sqrt{(D-T)^2 - (d+t)^2} \tag{14}$$

(Supplementary Material S6). Therefore, the total energy absorption of each aluminum foam cylinder in CSL model can be expressed as.

$$EA_{foam,\text{CSL}} = \begin{cases} \dfrac{\sigma_{pl}u_{foam}}{D-T}V_{eq,foam-\text{CSL}} & \left(u_{foam} \leqslant u_d\right) \\[2ex] \left[\dfrac{\sigma_{pl}u_{foam}}{D-T} + \dfrac{m}{n+1}\left(\dfrac{u_{foam}}{D-T} - \varepsilon_d\right)^{n+1}\right]V_{eq,foam-\text{CSL}} & \left(u_{foam} > u_d\right) \end{cases} \tag{15}$$

The lateral crushing force of each aluminum foam cylinder in CSL model $F_{foam,\text{CSL}}$ can be obtained by $F_{foam,\text{CSL}} = \mathrm{d}EA_{foam,\text{CSL}}/\mathrm{d}u_{foam}$ and approximated as.

$$F_{foam,\text{CSL}} = \begin{cases} \dfrac{\sigma_{pl}}{D-T}V_{eq,foam-\text{CSL}} & \left(u_{foam} \leqslant u_d\right) \\[2ex] \left[\dfrac{\sigma_{pl}}{D-T} + \dfrac{m}{D-T}\left(\dfrac{u_{foam}}{D-T} - \varepsilon_d\right)^{n}\right]V_{eq,foam-\text{CSL}} & \left(u_{foam} > u_d\right) \end{cases} \tag{16}$$

where the term $\mathrm{d}V_{eq,foam\text{-}\text{CSL}}/\mathrm{d}u_{foam}$ is ignored because its effect to $F_{foam,\text{CSL}}$ is limited. Similarly, the lateral crushing force of each foam cylinder in NCSL model $F_{foam,\text{NCSL}}$ can be expressed as.
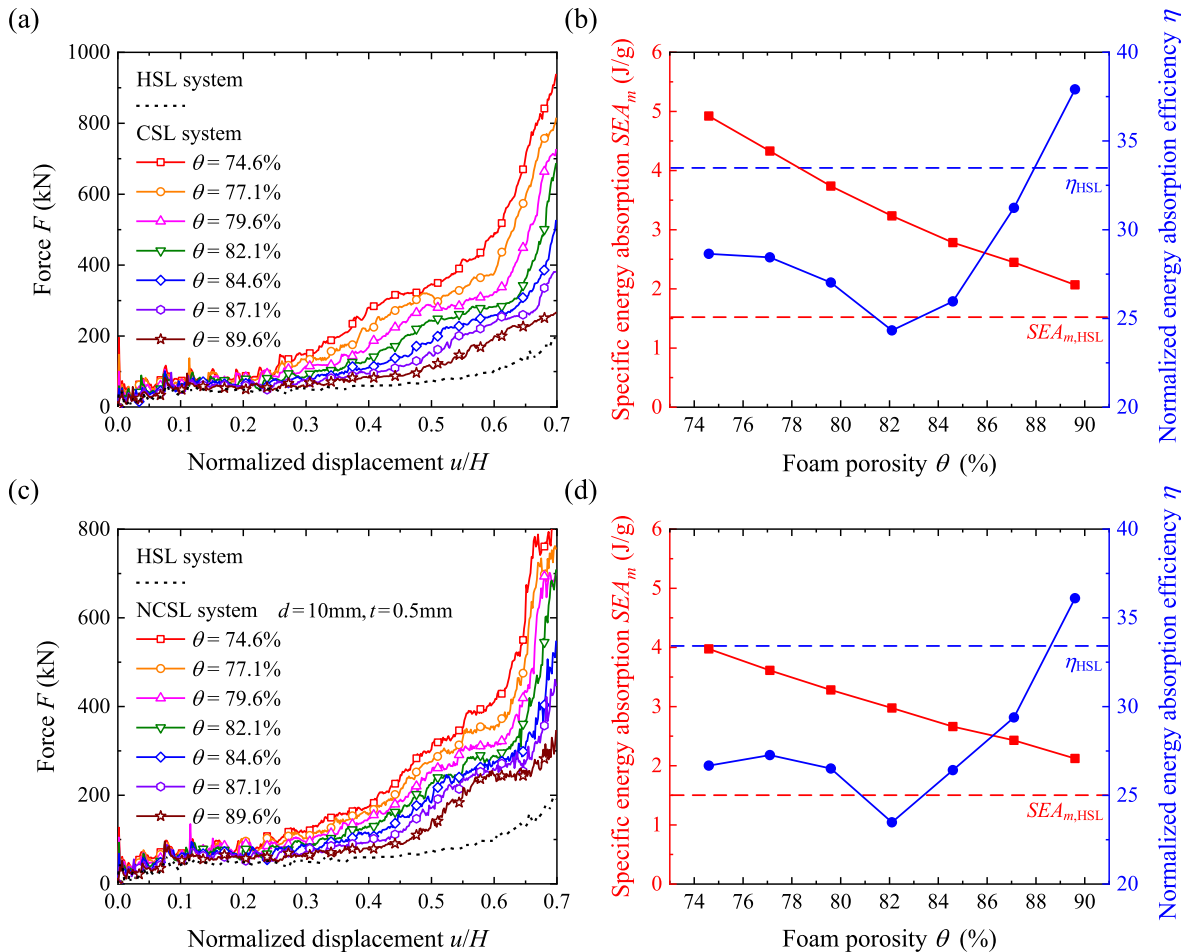

Fig. 6. The effects of the foam porosity on force–displacement curves and key performance indicators for (a)–(b) CSL system and (c)–(d) NCSL system.

$$F_{foam,NCSL} = \begin{cases} \dfrac{\sigma_{pl}}{D-T}V_{eq,foam-NCSL} & (u_{foam} \leqslant u_d) \\[2ex] \left[\dfrac{\sigma_{pl}}{D-T} + \dfrac{m}{D-T}\left(\dfrac{u_{foam}}{D-T} - \varepsilon_d\right)^n\right]V_{eq,foam-NCSL} & (u_{foam} > u_d) \end{cases}$$

(17)

The accuracy of the crushing force of single aluminum foam cylinder in CSL and NCSL models provided by Eqs. (16) and (17) are verified by simulation results (Supplementary Material S5).

Because the thin-walled outer tube is made of solid metal, it is approximately satisfied that.

$$u_{out} = u_{foam,CSL} = u_{foam,NCSL}$$

(18)

The crushing force of CSL model can thus be obtained by adding that of outer tube and aluminum foam filler due to weak interaction effect (Supplementary Material S4).

$$F_{CSL} = F_{out} + 2F_{foam,CSL}$$

(19)

where the expressions of F_{out} and $F_{foam,CSL}$ are provided in Eqs. (9) and (16), respectively.

For NCSL models, according to Eq. (1), it is satisfied that.

$$u_{in} = u_{out} - u_2 = u_{out} - (D - d - T + t)\theta$$

(20)

Based on Eq. (20), the Heaviside step function $H(x)$ is introduced here.

$$H(x) = \begin{cases} 0 & x \leqslant 0 \\ 1 & x > 0 \end{cases}$$

(21)

Therefore, the crushing force of NCSL model can be expressed by.

$$F_{NCSL} = F_{out} + 2F_{foam,NCSL} + H[u_{out} - (D - d - T + t)\theta] \cdot 2F_{in}$$

(22)

where the expressions of F_{out}, $F_{foam,NCSL}$ and F_{in} are provided in Eqs. (9), (17) and (10), respectively.

The theoretical crushing force of complete CSL and NCSL models obtained from Eqs. (19) and (22) are depicted as dashed lines with hollow symbols in Fig. 4, where the foam porosity θ is set ranging from 74.6% to 89.6%. The thickness of inner tube is adopted as 0.5 mm and other parameters are adopted the same as NCSL1 model in Section 2. As comparison, the simulation is also carried out and the results are displayed as solid symbols in Fig. 4, which coincide well with analytical solutions. It is demonstrated that the maximum crushing force of NCSL model can be controlled lower than CSL model by selecting suitable inner tube thickness, which is beneficial for improving the energy absorption efficiency. The theoretical model established in this section displays high accuracy, and can reveal the effect of deformation mechanism on energy absorption performance under static loading condition.
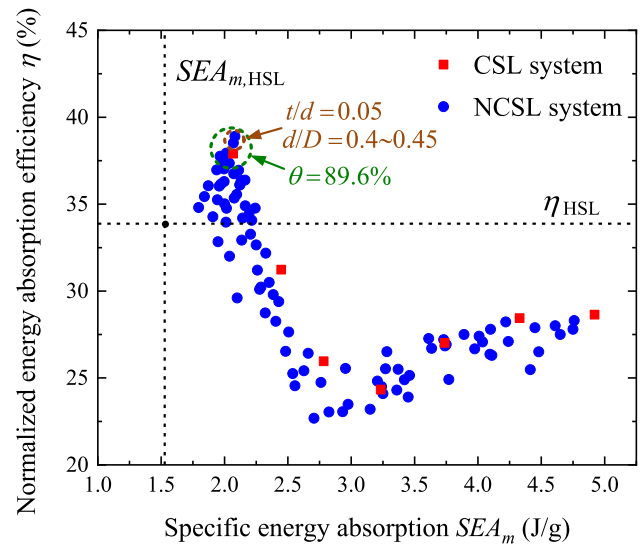

Fig. 8. SEA_m and η of all CSL and NCSL system models with $v = 20$ m/s.

Considering the actual requirements in engineering fields, parametric study of the newly-designed multiple-tube systems is then carried out under dynamic loading condition, which will be provided in Section 4.

4. Parametric study

In this section, more than a hundred FEM simulation models of CSL and NCSL multiple-tube systems are established and applied to dynamic loading condition, to reveal the effects of foam porosity, inner tube diameter and thickness on energy absorption performance. As comparison, the FEM simulation of HSL system is also carried out, and a guideline on the design of composite self-locked energy absorption systems is summarized. HSL, CSL and NCSL systems in this section are all assembled by 35 tubes, with the stacking arrangement and loading condition displayed in Fig. 5.

4.1. Effects of foam porosity θ

In this section, the foam porosity θ of the models is set ranging from 74.6% to 89.6%, with constitutive models provided in Supplementary Material S7. The geometric parameters of the outer tube are the same as Table 2, and the inner tubes of NCSL models satisfy $d = 10$ mm and $t = 0.5$ mm.

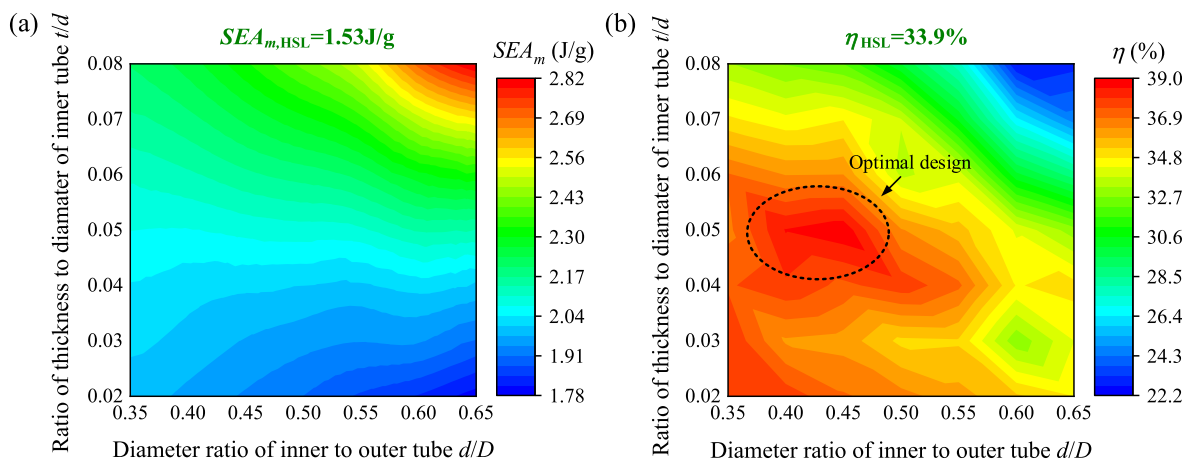The force–displacement curves of CSL systems with various θ are

Fig. 7. The effects of inner tube parameter on (a) SEA_m and (b) η of NCSL systems.

depicted in Fig. 6(a), and the specific energy absorption SEA_m and the normalized energy absorption efficiency η of the systems are calculated based on Eqs. (3)-(7) and displayed in Fig. 6(b). Besides, the force-–displacement curve and key performance indicators of HSL system are also illustrated in Fig. 5. From the results, the composite design can significantly enhance the load-carrying capacity, whilst the maximum crushing force is also increased. SEA_m is obviously enhanced when decreasing foam porosity, and the CSL system with $\theta\theta$ of 74.6% can achieve SEA_m of 4.92 J/g. η decreases with θ when $\theta < 82\%$ and increases with θ when $\theta > 82\%$, and η of CSL system is larger than HSL system only when $\theta > 88\%$. Therefore, taking both energy absorption capacity and efficiency into consideration, $\theta = 89.6\%$ can be approximated as optimal design for CSL system, which can display SEA_m and η respectively 35.4% and 11.9% larger than HSL model. Specially, for emergent engineering conditions where energy absorption capacity is overarching, θ can be adopted as about 74.6%, which can achieve SEA_m 3.22 times of that of HSL system in spite of weakening η of about 15.4%.

For NCSL systems, SEA_m can also be promoted when decreasing θ and the enhancement effect is relatively weaker than CSL systems, because the foam filler volume is smaller. Consistent with CSL systems, η of the NCSL system nearly decreases with θ when $\theta < 82\%$ and increases with $\theta\theta$ when $\theta > 82\%$, and η of NCSL system exceeds HSL system only when $\theta > 88\%$. As shown in Fig. 5(d), the NCSL system with $\theta = 89.6\%$ can achieve SEA_m and η respectively 39% and 6.6% larger than HSL model when $d = 10$ mm and $t = 0.5$ mm. Therefore, the energy absorption properties of NCSL systems can be increasingly promoted by adjusting d and t, which will be discussed in Section 4.2.

4.2. Effects of inner tube diameter d and thickness t

The effects of inner tube diameter d and thickness t on the energy absorption performance of NCSL systems are investigated here, where the foam porosity is selected as the optimal value of 89.6% based on conclusions of Section 4.1. Herein, the inner tube geometry is determined by normalized parameters, including diameter ratio of inner to outer tube d/D and ratio of thickness to diameter of inner tube t/d. Forty-nine FEM simulation models of NCSL systems are established here, with d/D ranging from 0.35 to 0.65 and t/d ranging from 0.02 to 0.08.

The effects of d/D and t/d on SEA_m and η of NCSL systems obtained from simulation results are depicted as contour plots, as shown in Fig. 7. As comparison, the energy absorption properties of HSL system obtained from FEM simulation are also symbolled. From the results in Fig. 7(a), SEA_m significantly increases with t/d, especially when d/D is relatively

Table 5
Details of the three typical impact loading conditions adopted in Section 5.

Loading mode	Impact energy E (kJ)	Mass M_0 (kg)	Initial velocity v_0 (m/s)
Low-speed	20	100	20
Medium-speed	20	25	40
High-speed	20	11.1	60

large. Moreover, SEA_m decreases with d/D when $t/d \leq 0.04$ and increases with d/D when $t/d \geq 0.05$. It can be seen that NCSL systems display energy absorption capacity much larger than HSL system, and the enhancing effect can exceed 50% when $t/d \geq 0.05$. As shown in Fig. 7(b), the systems with relatively large t/d and d/D exhibits weak energy absorption efficiency, because the stiffness of inner tubes is too large. Specially, NCSL systems display maximum efficiency of about 38.89% when $t/d = 0.05$ and $0.4 \leq d/D \leq 0.45$, which is 14.72% larger than that of HSL system. Therefore, the comprehensive performance can be enhanced by properly designing the fillers, and $t/d = 0.05$ and $0.4 \leq d/D \leq 0.45$ are adopted as the optimal design considering both energy absorption capacity and efficiency.

4.3. Comparison of CSL and NCSL systems with HSL system

To reveal the combined effect of aluminum foam filler and inner tubes to energy absorption properties, the simulation results of more than a hundred system models are summarized in Fig. 8, where foam porosity θ, diameter ratio of inner to outer tube d/D and ratio of thickness to diameter of inner tube t/d are respectively selected from 74.6% to 89.6%, 0.35 to 0.65 and 0.02 to 0.08. As a contrast, the energy absorption properties of HSL system obtained from FEM simulation are depicted as black dashed lines here. The two black dashed lines divide the indicator space into four subspaces, and the desired system model should have the energy absorption properties in the upper right subspace, indicating the improvement in both capacity and efficiency compared with traditional non-filling model. From the results, CSL and NCSL system models with $\theta = 89.6\%$ as marked in dashed green circle of Fig. 8 exhibit best comprehensive properties, which is consistent with the observations in Section 4.1. Specially, NCSL system models display extreme superior properties after geometry optimization, and the optimal design for inner tubes is $t/d = 0.05$ and $d/D = 0.4$–0.45, which coincides well with the results of Section 4.2. Taking both convenience and properties into consideration, CSL system model with $\theta = 89.6\%$ and NCSL system models with $\theta = 89.6\%$, $t/d = 0.05$ and $d/D = 0.4$–0.45 can
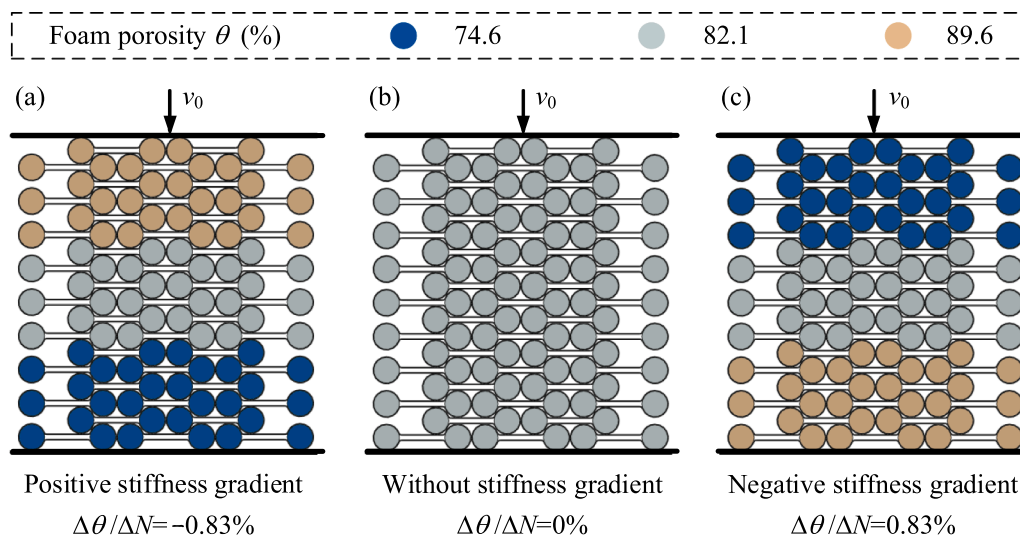

Fig. 9. Initial configurations of CSL systems with various graded design in Section 5: (a) positive stiffness gradient, (b) without stiffness gradient and (c) negative stiffness gradient.
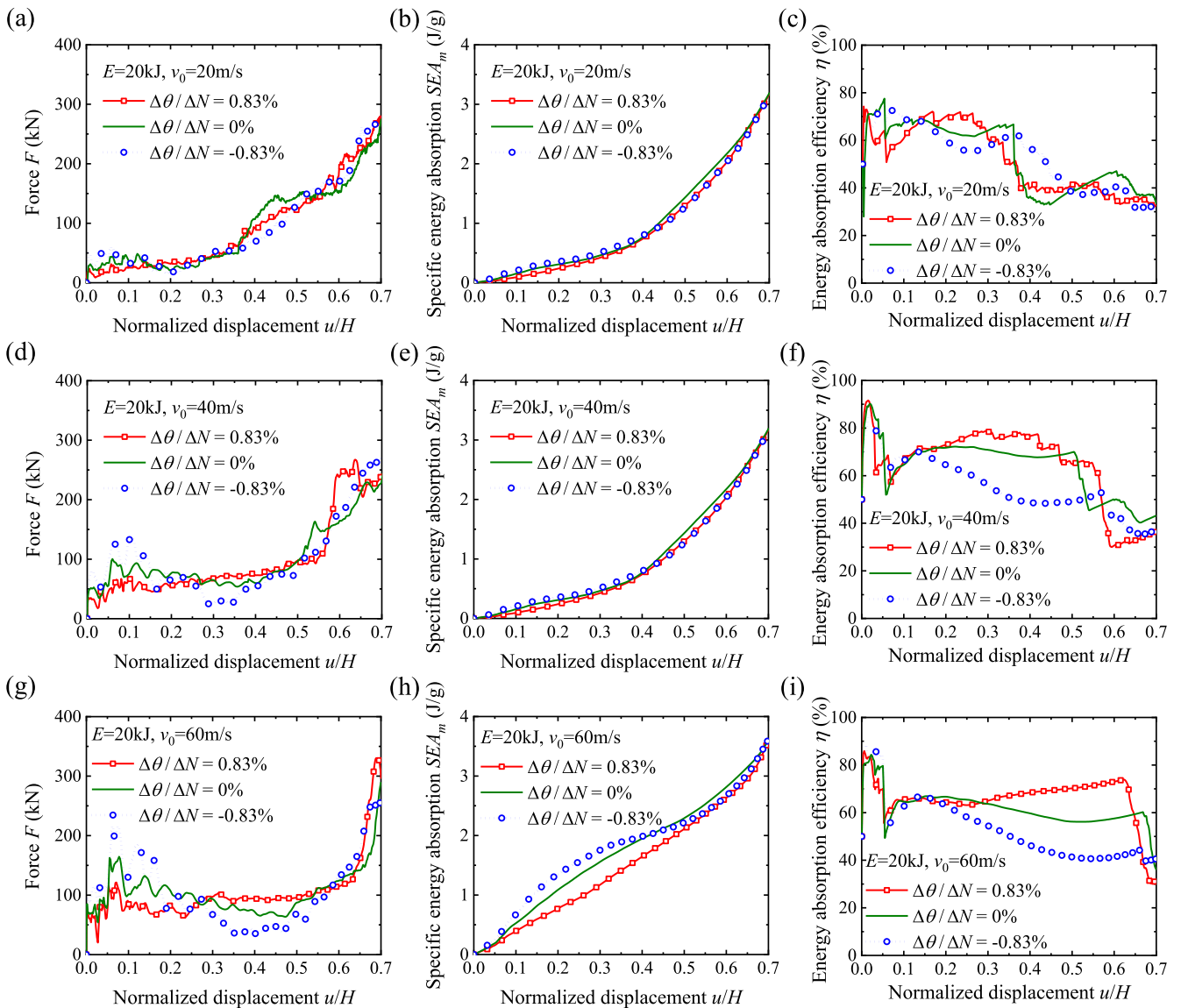
Fig. 10. Force-displacement curves and key performance indicators of CSL system models with various graded design under impact loading with various crushing velocities.

be approximated as the optimal design in engineering applications, which can respectively promote SEA_m and η by at least 35.3% and 11.9%. The results summarized in this section is based on the dynamic loading condition with v = 20 m/s, and it is proven that the conclusion of optimal design here is suitable for other dynamic condition.

5. Functionally graded design

Due to the convenience of discretely assembling, the proposed multiple-tube systems can easily improve the dynamic mechanical performance in practical applications by functionally graded design [28], where the stiffness distribution can be controlled by adjusting the foam porosity arrangement, enabling the discrete body to display the expected properties of continuum body.

In this section, a series of CSL system models with various foam porosity gradients are established as instances to reveal the effect of functionally graded design, of which the layer number is 18 and total tube number is 45, as shown in Fig. 9. The foam porosity is set as constant every six layers, and the integral tube thickness of each region is changed linearly. The average foam porosity of the systems is all set as 82.1%, and the total mass and height of all systems respectively equal

5.13 kg and 254.3 mm. The porosity gradients $\Delta\theta/\Delta N$ are set as −0.83%, 0 and 0.83% here as shown in Fig. 9, where $\Delta\theta/\Delta N$ is defined as the foam porosity span divided by layer number of the system, representing the systems with positive stiffness gradient, without stiffness gradient and with negative stiffness gradient, respectively. The thickness of outer tubes *T* is set as 0.5 mm to enhance the effect of the foam filler, and other parameters are the same as Section 4.1.

Based on the calculation result of total energy absorption *EA* in Section 4.1, the loading plate with the impact energy *E* of 20 kJ is imposed to crush the systems. Three typical loads with same impact energy and initial velocities of 20 m/s, 40 m/s and 60 m/s are adopted as shown in Table 5, respectively representing low-speed, medium-speed and high-speed loading conditions.

5.1. Low-speed loading condition

The systems with various stiffness graded designs display different deformed configurations under same loading condition, bringing in significant effect on force–displacement curve characteristics (Supplementary Material S8). The force–displacement curves of CSL system models with various graded design under impact loading with $v_0 = 20$

m/s are depicted in Fig. 10(a), with SEA_m and η respectively calculated and displayed in Fig. 10(b) and (c). Due to the stiffness difference of the regions near the loading plate, the system with positive gradient design displays weakest initial impact force peak and the system with negative gradient design displays strongest initial impact force peak. However, because the loading velocity is relatively small, the dynamic response is not intense and the force is increasing gently with the crushing displacement, and accordingly, the damage of the initial impact force peak can be neglected. Due to same average stiffness, the specific energy absorption SEA_m of the three systems is almost equaling during the deformation process. From the results in Fig. 10(c), there is no apparent quality difference between η of the systems with various graded design. Therefore, the effect of the stiffness graded design of the proposed system is not significant in low-speed loading condition, and the energy absorption performance is mainly dominated by average stiffness.

5.2. Medium-speed loading condition

For the loading condition with $v_0 = 40$ m/s, the deformation process of the three systems is almost the same as that of Section 5.1, but the equivalent plastic strain level difference between the systems is more distinct on account of the increasing crushing velocity. The force–displacement curves of the models with various graded design under impact loading with $v_0 = 40$ m/s are depicted in Fig. 10(d), with SEA_m and η respectively calculated and displayed in Fig. 10(e) and (f). Similar as the dynamic response under low-speed loading condition, the system with negative stiffness gradient exhibits strong initial force peak and appears low value after that, and the system with positive stiffness gradient displays more stable force–displacement curve. As shown in Fig. 10(f), the normalized energy absorption efficiency η of the system with positive stiffness gradient maintains high level during the deformation, and thus the system can be imposed with positive stiffness gradient in engineering fields to reply to medium-speed loading condition, to attenuate the initial impact force peak and improve comprehensive energy-absorbing performance.

5.3. High-speed loading condition

The force–displacement curves of the models with various graded design under impact loading with $v_0 = 60$ m/s are depicted in Fig. 10(g), with SEA_m and η displayed in Fig. 10(h) and (i), respectively. The initial force peak of the systems with the negative stiffness gradient and uniform stiffness is much more sharp due to the increase of the loading velocity, resulting in great damage to energy absorption efficiency based on Eq. (7). Taking both energy absorption capacity and efficiency into consideration, the system with positive stiffness gradient design is selected as the optimal design to apply to high-speed loading condition in this paper.

As a summary, the proposed systems can easily improve the dynamic mechanical performance by functionally graded design due to the convenience of discretely assembling, and the system with positive stiffness gradient can be applied as the optimal design to apply to various engineering conditions. This conclusion is different from part of previous studies, because the force–displacement curves of the self-locked systems are comparatively stable due to the interspaces among energy-absorbing elements, which had been proven in high-speed impact experiment [20], and thus the damage caused by initial force peak under dynamic loading condition is more obvious.

6. Conclusion

In this paper, composite self-locked (CSL) and nested composite self-locked (NCSL) energy absorption systems were proposed, and experiments, FEM simulations and theoretical analysis were carried out to reveal their energy-absorbing response. Specific conclusions are as follows.

(1) The deformation process of CSL and NCSL systems could be divided into three and four phases, respectively, and the energy absorption capacity was significantly enhanced. Although the maximum crushing force was also increased, it was proven that the energy-absorbing efficiency maintained high level by suitable design of aluminum foam and inner tubes.
(2) The analytical solutions of the crushing force of CSL and NCSL models were derived based on plastic hinge analysis and energy method, revealing the effect of deformation mechanism on static mechanical response, and its accuracy was validated by experiments and FEM simulation.
(3) Parametric study of multiple-tube systems was carried out, to reveal the effect of foam porosity and inner tube parameter under dynamic loads. The optimal values of $\theta\theta$, d/D and t/d were respectively 89.6%, 0.4–0.45 and 0.05, promoting capacity and efficiency by 35.3% and 11.9%.
(4) The proposed systems could easily enhance the dynamic mechanical performance in engineering applications by functionally graded design due to the convenience of discretely assembling, and the system with positive stiffness gradient was the optimal design.

CRediT authorship contribution statement

Jinxin Pan: Methodology, Software, Formal analysis, Data curation, Writing – original draft. **Weiyu Zhu:** Investigation, Software, Data curation, Writing – original draft. **Kuijian Yang:** Conceptualization, Methodology, Validation, Writing – review & editing, Funding acquisition, Supervision. **Lingling Hu:** Writing – review & editing, Funding acquisition, Supervision. **Yuli Chen:** Writing – review & editing, Supervision.

Declaration of Competing Interest

The authors declare that they have no known competing financial interests or personal relationships that could have appeared to influence the work reported in this paper.

Appendix A. Supplementary material

Supplementary data to this article can be found online at https://doi.org/10.1016/j.compstruct.2022.115686.

References

[1] Lu G, Yu T. Energy absorption of structures and materials. Cambridge: Woodhead Publishing Ltd; 2003.
[2] Alghamdi A. Collapsible impact energy absorbers: an overview. Thin-walled Struct 2001;39:189–213.
[3] Olabi AG, Morris E, Hashmi M. Metallic tube type energy absorbers: a synopsis. Thin-walled Struct 2007;45:706–26.
[4] Abramowicz W. Thin-walled structures as impact energy absorbers. Thin-walled Struct 2003;41:91–107.
[5] Xu X, Zhao Z, Wang W, Tong Z, Zhou Z, Lim CW. A novel design of thin-walled energy absorption structures with local surface nanocrystallization. Thin-walled Struct 2021;160:107337.
[6] Liu Y, Xiong F, Yang K, Chen Y. A novel omnidirectional self-locked energy absorption system inspired by windmill. J Appl Mech 2020;87:085001.
[7] Ghasemi A, Shakeri M, Vanini SAS. A multi-objective optimization of energy absorption properties of thin-walled circular tube with combined bar extrusion under quasi-static axial loading: experiments and numerical simulation. Int J Mech Sci 2020;180:105691.

[8] Zhang B, Wang L, Zhang J, Jiang Y, Wang W, Wu G. Deformation and energy absorption properties of cenosphere/aluminum syntactic foam-filled circular tubes under lateral quasi-static compression. Int J Mech Sci 2021;192:106126.

[9] Li S, Yu B, Karagiozova D, Liu Z, Lu G, Wang Z. Experimental, numerical, and theoretical studies of the response of short cylindrical stainless steel tubes under lateral air blast loading. Int J Impact Eng 2019;124:48–60.

[10] Xing J, Xu P, Yao S, Zhao H, Zhao Z, Wang Z. Study on the layout strategy of diaphragms to enhance the energy absorption of thin-walled square tubes. Structures 2021;29:294–304.

[11] Wang H, Yang J, Liu H, Sun Y, Yu T. Internally nested circular tube system subjected to lateral impact loading. Thin-walled Struct 2015;91:72–81.

[12] Yang K, Chen Y, Liu S, Qiao C, Yang J. Internally nested self-locked tube system for energy absorption. Thin-walled Struct 2017;119:371–84.

[13] Hu D, Wang Y, Song B, Dang L, Zhang Z. Energy-absorption characteristics of a bionic honeycomb tubular nested structure inspired by bamboo under axial crushing. Compos B Eng 2019;162:21–32.

[14] Islam MA, Kader MA, Hazell PJ, Escobedo JP, Brown AD, Saadatfar M. Effects of impactor shape on the deformation and energy absorption of closed cell aluminium foams under low velocity impact. Mater Des 2020;191:108599.

[15] Sun Z, Hu X, Sun S, Chen H. Energy-absorption enhancement in carbon-fiber aluminum-foam sandwich structures from short aramid-fiber interfacial reinforcement. Compos Sci Technol 2013;77:14–21.

[16] Meredith J, Ebsworth R, Coles SR, Wood BM, Kirwan K. Natural fibre composite energy absorption structures. Compos Sci Technol 2012;72:211–7.

[17] Huang W, Xu H, Fan Z, Jiang W, Liu J. Dynamic failure of ceramic particle reinforced foam-filled composite lattice core. Compos Sci Technol 2020;193: 108143.

[18] Jenett B, Cameron C, Tourlomousis F, Rubio AP, Gershenfeld N. Discretely assembled mechanical metamaterials. Sci Adv 2020;6:eabc9943.

[19] Chen Y, Qiao C, Qiu X, Zhao S, Zhen C, Liu B. A novel self-locked energy absorbing system. J Mech Phys Solids 2016;87:130–49.

[20] Yang K, Qin Q, Zhai Z, Qiao C, Chen Y, Yang J. Dynamic response of self-locked energy absorption system under impact loadings. Int J Impact Eng 2018;122: 209–27.

[21] Baroutaji A, Gilchrist M, Smyth D, Olabi A-G. Crush analysis and multi-objective optimization design for circular tube under quasi-static lateral loading. Thin-walled Struct 2015;86:121–31.

[22] Zhou C, Li T, Ming S, Song Z, Wang B. Improving the energy absorption of cruciform with large global slenderness ratio by kirigami approach and welding technology. J Appl Mech 2019;86:081004.

[23] Xiang X, Zou S, Ha NS, Lu G, Kong I. Energy absorption of bio-inspired multi-layered graded foam-filled structures under axial crushing. Compos B Eng 2020; 198:108216.

[24] Li S, Guo X, Liao J, Li Q, Sun G. Crushing analysis and design optimization for foam-filled aluminum/CFRP hybrid tube against transverse impact. Compos B Eng 2020;196:108029.

[25] Yang K, Qiao C, Xiong F, Zhang L, Wu Z, Chen Y. Theoretical investigation on the energy absorption of ellipse-shaped self-locked tubes. Sci China Phys Mech Astron 2020;63:270000.

[26] DeRuntz JA, Hodge PG. Crushing of a tube between rigid plates. J Appl Mech 1963; 30:391–5.

[27] Yan L, Yu B, Han B, Chen C, Zhang Q, Lu T. Compressive strength and energy absorption of sandwich panels with aluminum foam-filled corrugated cores. Compos Sci Technol 2013;86:142–8.

[28] Liu H, Zhang Z, Liu H, Yang J, Lin H. Theoretical investigation on impact resistance and energy absorption of foams with nonlinearly varying density. Compos B Eng 2017;116:76–88.